Hierarchical $NiCo_2S_4$ Nanowire Arrays Supported on Ni Foam: An Efficient and Durable Bifunctional Electrocatalyst for Oxygen and Hydrogen Evolution Reactions

*Arumugam Sivanantham, Pandian Ganesan, and Sangaraju Shanmugam**

Dedicated to Prof. Tetsuya Osaka on the occasion of his 70th birthday.

A recent approach for solar-to-hydrogen generation has been water electrolysis using efficient, stable, and inexpensive bifunctional electrocatalysts within strong electrolytes. Herein, the direct growth of 1D $NiCo_2S_4$ nanowire (NW) arrays on a 3D Ni foam (NF) is described. This $NiCo_2S_4$ NW/NF array functions as an efficient bifunctional electrocatalyst for overall water splitting with excellent activity and stability. The 3D-Ni foam facilitates the directional growth, exposing more active sites of the catalyst for electrochemical reactions at the electrode–electrolyte interface. The binder-free, self-made $NiCo_2S_4$ NW/NF electrode delivers a hydrogen production current density of 10 mA cm^{-2} at an overpotential of 260 mV for the oxygen evolution reaction and at 210 mV (versus a reversible hydrogen electrode) for the hydrogen evolution reaction in 1 M KOH. This highly active and stable bifunctional electrocatalyst enables the preparation of an alkaline water electrolyzer that could deliver 10 mA cm^{-2} under a cell voltage of 1.63 V. Because the nonprecious-metal $NiCo_2S_4$ NW/NF foam-based electrodes afford the vigorous and continuous evolution of both H_2 and O_2 at 1.68 V, generated using a solar panel, they appear to be promising water splitting devices for large-scale solar-to-hydrogen generation.

1. Introduction

Increasing energy demands and the inevitability of fossil fuel depletion are encouraging the search for eco-friendly, renewable, and clean alternative energy resources and for new methods for the efficient extraction of energy.[1,2] Molecular hydrogen is an ideal energy sector for overcoming future energy anxieties, due to its outstanding energy density, high energy conversion efficiency, and environmental friendliness.[3,4] Electrochemical water splitting is a well-established commercial technology for producing clean hydrogen energy with zero carbon emission.[5,6] Although electrolyzers coupled to photovoltaic modules for direct solar-to-hydrogen generation should be excellent energy conversion systems,[7,8] producing hydrogen on large scales with high purity remains difficult because its strong uphill reaction requires a potential of ≈1.8–2.0 V, significantly greater than the theoretical value of 1.23 V.[9,10] This large overpotential required in an electrolyzer arises from a sluggish anodic oxygen evolution reaction (OER) and a fairly facile cathodic hydrogen evolution reaction (HER). This overpotential is related to the activity of the electrocatalyst during such bifunctional performance. Therefore, the most active electrocatalysts must be implemented to minimize the overpotentials at both electrodes to ensure that the process becomes more energy-efficient.[11,12] At present, the state-of-the-art electrocatalysts for OER and HER are Ir- and Ru-based materials and Pt-group metals, respectively.[13,14] Nevertheless, the scarcity, high cost, low bifunctionality, and poor stability of these noble metal-based catalysts limit their large-scale application. Accordingly, we have been motivated to design highly active, highly durable, inexpensive, and readily available bifunctional electrocatalysts for use as efficient electrode materials for OER and HER.

Recently, non-noble transition metal (e.g., Ni, Co, Fe, Mo, and W)-based oxides have been explored extensively as OER electrocatalysts on various supports.[15–19] Most of the oxide-based materials reported to date have not been active for both OER and HER in the same electrolyte environment (limited by an inappropriate crystal structure, low conductivity, or low band gap), hampering their applicability in the overall water splitting process. Cheng et al. prepared $NiCo_2O_4$ on carbon nanotubes (CNTs) nanostructures that exhibited good electrocatalytic OER activity in 1 M KOH.[2] More notably, Chen et al. examined the OER performance of $NiCo_2O_4$ nanowire cores covered by $NiCo_2O_4$ nanoflake shells; devices featuring these core/shell nanostructures afforded a current density of 10 mA cm^{-2} when operated at 1.55 V.[20] To minimize the overpotential for overall water splitting, any electrocatalyst must be highly active for both OER and HER reactions in both strongly acidic and alkaline electrolyte solutions. This characteristic is highly challenging with earth-abundant non-noble metal catalysts, which

A. Sivanantham, P. Ganesan, Prof. S. Shanmugam
Department of Energy Systems Engineering
Daegu Gyeongbuk Institute of Science
& Technology (DGIST)
Daegu 42988, Republic of Korea
E-mail: sangarajus@dgist.ac.kr

DOI: 10.1002/adfm.201600566

can display inactivity or poor stability in extremely strong electrolyte environments. Because of the high solubility of catalysts in strongly acidic water splitting, alkaline water splitting has emerged as a strong candidate for viable large-scale mass production of hydrogen.[21,22] Therefore, catalysts capable of catalyzing both OER and HER reactions in strongly alkaline electrolytes should be promising materials for minimizing the cost of water splitting devices, and also simplifying the requirement for diverse equipment and process. Thus, we were attracted to exploring novel electrocatalysts exhibiting both bifunctional activity and good stability in the same electrolyte environment.

Recently, transition metal sulfides, phosphides, and hydroxides have been investigated as either OER or HER electrocatalysts.[1,23–25] Noticeably, the morphology of the catalyst, such as nanowires (NWs), nanorods have more attention in either OER or HER.[26–28] Some of the reported catalysts have been demonstrated as bifunctional electrocatalysts that decrease the overpotential in full water splitting reactions. For example, Liu et al. found that carbon cloth (CC)-supported $NiCo_2S_4$ could afford a current density of 10 mA cm^{-2} at 1.68 V in a two-electrode system.[29] Soon thereafter, Zhu et al. reported an NiS on Ni foam (NF) catalyst that achieved a current density of 10 mA cm^{-2} at a cell voltage of 1.64 V.[21] Shi et al. demonstrated the bifunctional activity of Ni_3Se_2 on Cu foil; in a two-electrode water splitting system it delivered a current density of 10 mA cm^{-2} at 1.65 V.[30] Even though these catalysts displayed promising OER activity, they must also exhibit stability if they are to be used as durable catalysts in the strongly alkaline environments found in real large-scale applications. Binary compounds typically have less structural stability than ternary compounds during electrochemical processes. Thus, despite great progress in preparing bifunctional catalysts, their activity and stability remain unsatisfactory for overall water splitting, stimulating further explorations of new electrocatalysts with higher activity, greater stability, and lower cost.

Several feasible strategies for optimizing the catalytic activity of electrocatalysts in overall water splitting have been developed, including (i) using nanostructures to increase the electrochemical active surface area and selectively expose more active sites,[6] (ii) preparing spinel nanostructures that are more stable in strong electrolyte environments,[2] (iii) applying large anions to expose more cationic active sites with multivalent states and also increase the electrical conductivity of the electrocatalysts,[31] (iv) hybridizing the electrocatalysts with various substrates (e.g., NF, Ti foil, and CNTs) to ensure uniform growth of 1D nanostructures with large surface areas and greater surface roughness to increase the number of active sites, facilitate electrolyte movement (greater wettability), and suppress the aggregation of active sites through an anchoring effect, while decreasing the contact resistance and increasing the electrical conductivity.[32] Nevertheless, it remains very challenging to develop a single advanced catalyst by taking advantage of all of these strategies in a cost-effective manner. To the best of our knowledge, there have been no previous reports of spinel $NiCo_2S_4$ nanostructures grown directly on 3D Ni foam through simple, inexpensive hydrothermal approaches nor their exploration as bifunctional electrocatalysts for overall water splitting.

Herein, we describe the successful growth of $NiCo_2S_4$ nanowire arrays on an Ni foam ($NiCo_2S_4$ NW/NF) using a pressurized hydrothermal method; this material acts as an efficient bifunctional electrocatalyst for both OER and HER with good durability in alkaline environments. Through structural studies we confirmed the formation of the $NiCo_2S_4$ nanowire arrays on the Ni foam support, with X-ray photoelectron spectroscopy (XPS) peaks revealing the presence of multiple oxidation states of the active species in the crystal structure. This $NiCo_2S_4$ NW/NF structure exhibited lower overpotentials of 260 and 210 mV at a current density of 10 mA cm^{-2} for OER and HER, respectively, in 1 M KOH electrolyte solution, significantly superior to the activities of $NiCo_2S_4$, Ni_3S_2/NF, and $NiCo_2O_4$/NF. Taking advantage of this excellent bifunctional activity, we prepared a two-electrode water electrolyzer in an alkaline electrolyte that, in a chrono-potentiometric stability test, displayed a constant water splitting current density of 10 mA cm^{-2} for 50 h. Moreover, herein we demonstrate solar-to-hydrogen generation at 1.68 V in a two-electrode set-up.

2. Results and Discussion

Figure 1 displays a schematic representation of the in situ growth of hierarchical $NiCo_2S_4$ nanowire arrays on a Ni foam substrate using a two-step hydrothermal method. The Ni foam was selected as a substrate because of its excellent electrical conductivity, 3D macroporous structure (Figure 1a), and various electrochemical features toward our application. The high purity Ni foam (>99.99%, 80 μm) with a dimension of 2 cm × 3 cm was used as a substrate with a porosity of 80–110 pores per inch. The average diameter of each pore is about 150 μm. In the first step, we grew uniform Ni-Co-carbonates hydroxide nanowire arrays on a 3D conductive Ni foam (2 cm × 3 cm) through hydrothermal treatment of Ni^{2+} and Co^{2+} with water in the presence of urea at 120 °C for 6 h in an electrical oven.[33] Next, the Ni-Co-carbonates hydroxide nanowire arrays were completely converted into spinel $NiCo_2S_4$ nanowire arrays, according to a coordinating etching and precipitating process in a sodium sulfide environment at 160 °C for 8 h (Figure 1b). In this second step, during the anion exchange reaction, the active sulfur anions (S^{2-}) released from sodium sulfide replaced the CO_3^{2-} and OH^- anions of the Ni-Co-carbonates hydroxide nanowire arrays to form hierarchical $NiCo_2S_4$ nanowire arrays on the Ni foam (for more details, see the Materials and Methods section). The exchanged CO_3^{2-} and OH^- anions reacted with H^+ ions in the solution to form CO_2 and H_2O. The Ni foam acted as a skeleton that anchored the $NiCo_2S_4$ nanowire arrays. The resulting Ni foam surface was completely black in color without any patches (for a clear image, see Figure S1, Supporting Information), suggesting the uniform formation of $NiCo_2S_4$ nanowire arrays on the Ni foam (Figure 1c). Field emission scanning electron microscope (FESEM) images confirmed the formation of nanowire arrays in a 3D structure (Figure 1c).

Figure 2 presents X-ray diffraction (XRD) patterns of various hydrothermally prepared electrocatalysts. In Figure 2a, the diffraction peaks of $NiCo_2(CO_3)_{1.5}(OH)_3$ with orthorhombic phase (after first step in hydrothermal process) can be well matched with $Co(CO_3)_{0.5}OH$ (JCPDS: 48-0083), because the

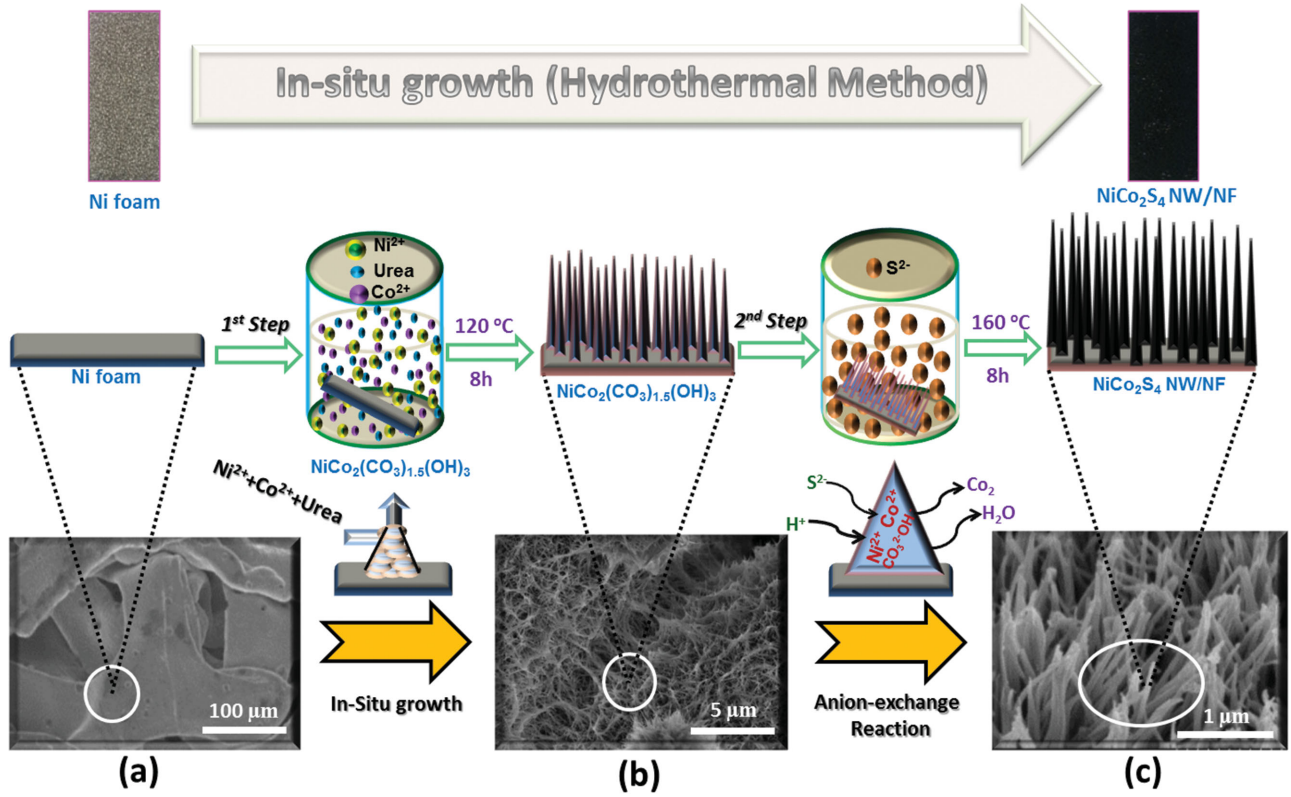

Figure 1. Schematic illustration of the formation of $NiCo_2S_4$ nanowire arrays on Ni foam and their corresponding morphology. a) Bare Ni foam substrate, b) in situ growth of $NiCo_2(Co_3)_{1.5}(OH)_3$ nanowire arrays on Ni foam (1st step), c) anion exchange reaction with complete growth of hierarchical $NiCo_2S_4$ nanowire arrays on Ni foam (2nd step) using hydrothermal method.

partial replacement of Co ions by Ni ions does not change the crystal structure, which only make a slight changes in the lattice parameters.[34,35] The diffraction peaks at values of 2θ of 26.7°, 31.4°, 31.8°, 47.2°, 50.2°, and 55° can be indexed to the (220), (113), (004), (224), (115), and (044) planes, respectively, of $NiCo_2S_4$ (Figure 2b) having cubic phase (JCPDS: 98-062-4474). The diffraction patterns for $NiCo_2S_4$ NW/NF (Figure 2c) are similar to that of $NiCo_2S_4$ (Figure 2b) with two strong characteristic peaks at 44.2° and 52° arising from the Ni foam (JCPDS: 98-004-3397). The peak at 21.7° (marked with an asterisk) is due to the small amount of Ni_3S_2 formed during the second step. This Ni_3S_2 impurity might have formed when the Ni foam was immersed in the sodium sulfide solution. Figure 2d displays obvious rhombohedral phase peaks corresponding to the formation of Ni_3S_2/NF (JCPDS: 00-044-1418). The diffraction peaks in Figure 2e confirm the formation of a cubic $NiCo_2O_4$/NF phase (JCPDS: 01-073-1702) without any impurities.

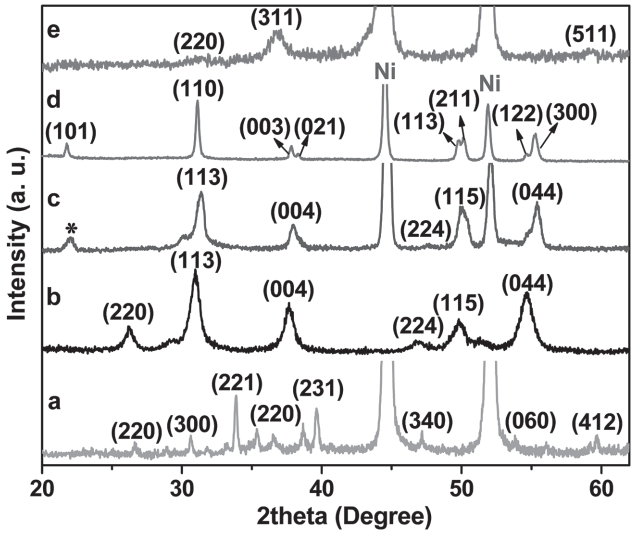

Figure 2. XRD patterns of a) $NiCo_2(CO_3)_{1.5}(OH)_3$, b) $NiCo_2S_4$, c) $NiCo_2S_4$ NW/NF, d) Ni_3S_2/NF, and e) $NiCo_2O_4$/NF.

Figure 3 displays FESEM images of the catalysts prepared with and without the Ni foam support. Figure 3a–d reveals the presence of aggregated large $NiCo_2S_4$ clusters of irregular shape formed in the absence of the foam. This irregular aggregated morphology suggested that the Ni foam substrate was necessary for the growth of 1D nanostructures. Figure 3e–h presents images of the $NiCo_2S_4$ grown on the Ni foam. Figure 3e reveals that the whole Ni foam substrate was covered closely and uniformly by the $NiCo_2S_4$ catalyst, forming a 3D hierarchical porous structure (Figure 3f). Figure 3g,h reveals that the $NiCo_2S_4$ nanowire arrays formed with sharp tips that had grown nearly vertical to the substrate. Furthermore, these $NiCo_2S_4$ nanowire arrays were well separated, with a mean diameter of ≈70 nm and a mean length of ≈1 µm along the directional growth. Each nanowire array had its own direct

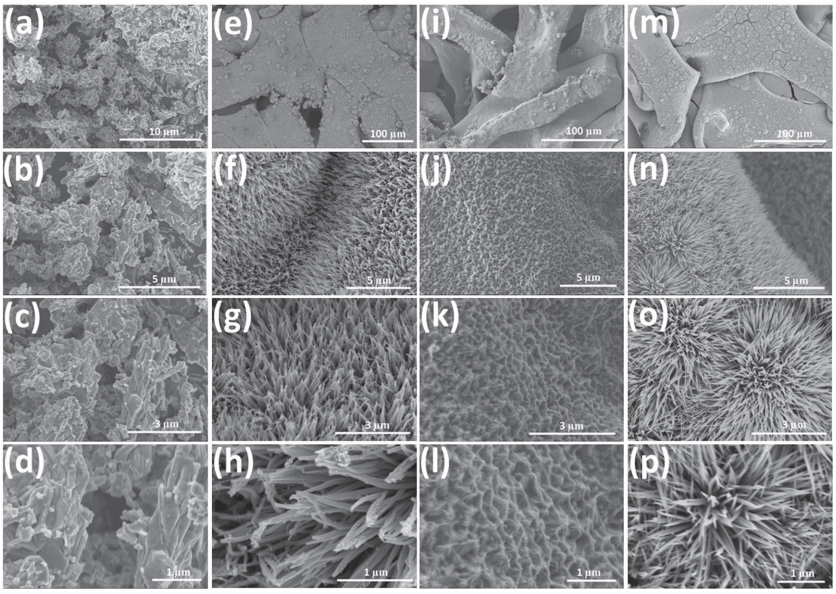

Figure 3. FESEM images of a–d) $NiCo_2S_4$, e–h) $NiCo_2S_4$ NW/NF, i–l) Ni_3S_2/NF, and m–p) $NiCo_2O_4$/NF.

contact with the surface of the current collector at the bottom, ensuring that it would effectively participate in the anodic and cathodic reactions. Another feature for proficient catalytic activity is strong adhesion with minimal contact resistance for efficient direct electron transport between the catalyst and the current collector.[36,37]

Similarly, we observed that Ni_3S_2 (Figure 3i–l) and $NiCo_2O_4$ (Figure 3m–p) had grown uniformly throughout the Ni foam without any aggregation on the surface. The $NiCo_2O_4$/NF structure featured nanowire arrays having a mean diameter of ≈80 nm and a mean length of ≈1 µm. By contrast, the Ni_3S_2/NF structure contained partially grown nanowire arrays, due to the insufficient reaction temperature and time. Thus, it is clear that the temperature required for Ni_3S_2/NF formation was higher than that for $NiCo_2S_4$ NW/NF.[38] From these morphological observations, we confirmed that the support played a major role in providing catalysts with high surface areas when using the in situ growth method. We suspected that, if the surface area were high, more catalyst elements would be actively involved in the electrochemical reactions, leading to improved catalytic activity.

We used transmission electron microscopy (TEM) to further investigate the morphology of the as-synthesized $NiCo_2S_4$ NW/NF (**Figure 4**). TEM images of $NiCo_2S_4$ nanowire arrays detached ultrasonically from the Ni foam substrate are presented in Figure 4a–c. Figure 4a reveals hierarchical $NiCo_2S_4$ nanowire arrays having a diameter of 70 nm, in good agreement with the FESEM results (Figure 3f). This unique hierarchical nanowire array structure would provide a large active surface area that could readily access electrolyte ions and increase the number of active sites for OER and HER. The high-resolution TEM (HRTEM) image of the nanowire arrays in Figure 4d reveals that the lattice planes had random orientations, consistent with the polycrystalline nature of the sample. The measured lattice spacings between two fringes in Figure 4d were 0.28 and 0.16 nm; we attribute them to the diffraction of the (113) and (044) lattice planes, respectively, of the $NiCo_2S_4$, in line with the XRD results. The corresponding selected-area electron diffraction (SAED) pattern (inset to Figure 4d) confirmed the polycrystalline nature of $NiCo_2S_4$ nanowire arrays. Scanning TEM and EDX elemental mapping (Figure 4e–h) revealed the superposition of the uniform spatial distribution of Ni, Co, and S atoms over the examined detection range at the surface of the $NiCo_2S_4$ nanowire arrays. Together, these results supported the notion of polycrystalline spinel $NiCo_2S_4$ nanowire arrays that might possess excellent OER and HER activities.

We used XPS to characterize the chemical valence states of the various elements in the $NiCo_2S_4$ NW/NF structure. **Figure 5** displays the typical fitted Co 2p, Ni 2p, and S 2p XPS spectra of the $NiCo_2S_4$ NW/NF, obtained using the Gaussian fitting method. As revealed in Figure 5a, the Co 2p XPS spectrum was best fitted with two spin-orbit doublets: one at 778.8 and

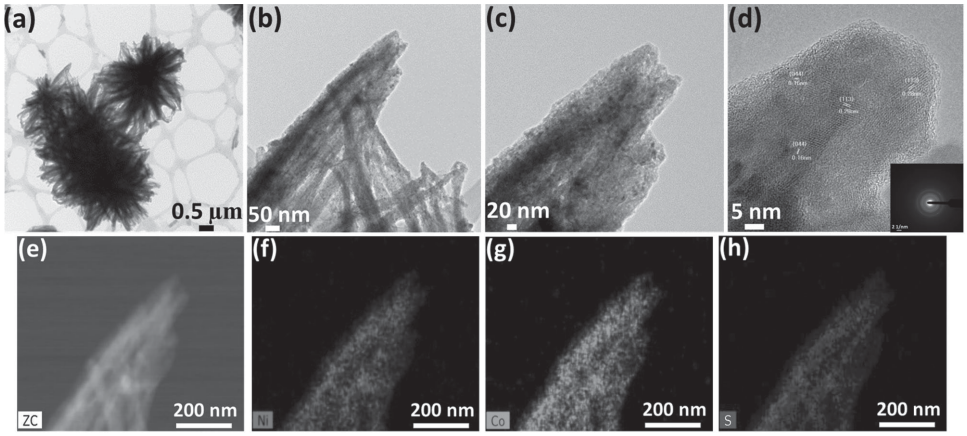

Figure 4. a–c) TEM images, d) HR-TEM image and SAED pattern (inset), and elemental mapping of $NiCo_2S_4$ NW/NF for e) ZC, f) Ni, g) Co, and h) S.

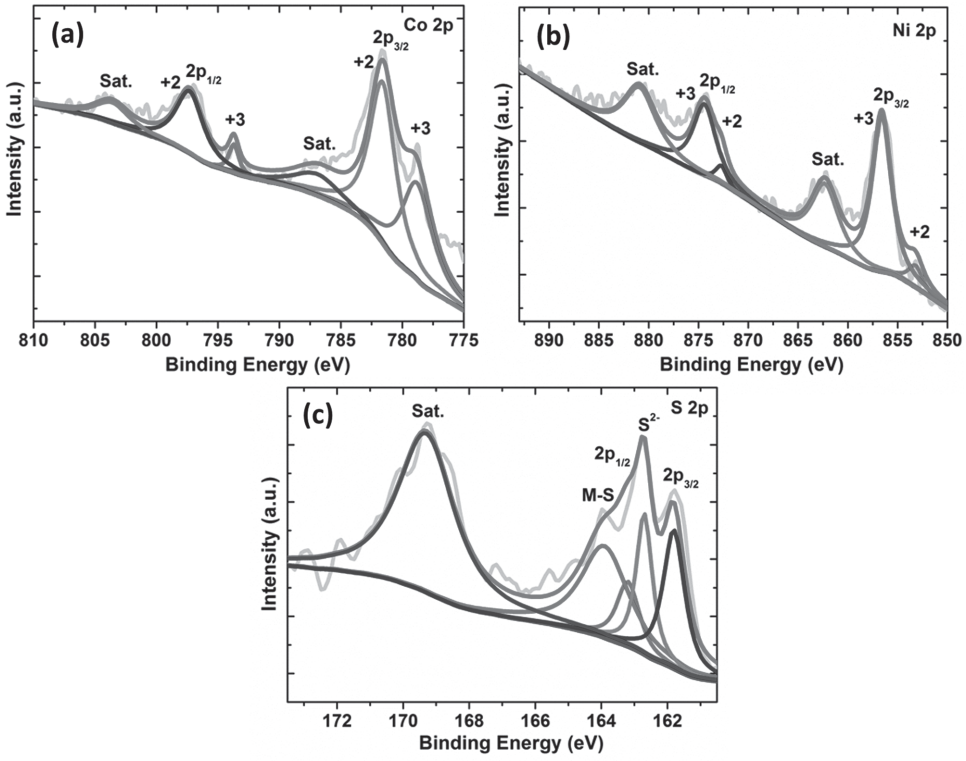

Figure 5. XPS spectra of a) Co 2p, b) Ni 2p, and c) S 2p for $NiCo_2S_4$ NW/NF (Sat. means shake-up satellites).

793.7 eV and the other at 781.6 and 797.3 eV, corresponding to spin-orbit splitting values of Co $2p_{1/2}$ and Co $2p_{3/2}$ of 15.1 eV and 16.3 eV, respectively, which can be ascribed to Co^{3+} and Co^{2+}, respectively.[34] The weak satellite peaks indicate that the majority of Co atoms were in the Co^{3+} state.[39] In Ni 2p XPS spectrum (Figure 5b), the binding energies at 853.2 eV for Ni $2p_{3/2}$ and 872.6 eV for Ni $2p_{1/2}$ are spin-orbit characteristics of Ni^{2+}, while the existing binding energies at 856.2 eV for Ni $2p_{3/2}$ and 874.4 eV for Ni $2p_{1/2}$ are spin-orbit characteristics of Ni^{3+}.[40] Likewise, an intense satellite peak suggested that the Ni^{2+} state was predominant in the Ni 2p spectra.[41] The S 2p spectrum (Figure 5c) was deconvoluted into four peaks and one shake-up satellite peak. The peaks at 163.1 and 161.8 eV correspond to S $2p_{3/2}$ and S $2p_{1/2}$ binding energies, respectively. The component peak at 163.8 eV is typical of a metal–sulfur (M–S) bond in the $NiCo_2S_4$ NW/NF material, while the other component peak present at 162.6 eV suggested the presence of sulfur ions in a low coordination state at the surface.[42] Thus, the XPS analysis confirmed that, near its surface, the sample had a composition of Co^{2+}, Co^{3+}, Ni^{2+}, and Ni^{3+} cations, M–S bonds, and S^{2-} anions. This result is consistent with the formation of a Ni–Co–S composite having a $NiCo_2S_4$ phase on a Ni foam, as revealed through XRD analysis (Figure 2).

Next, we assessed the electrocatalytic OER activity of the $NiCo_2S_4$ NW/NF in an alkaline solution (1 M KOH) using a standard three-electrode system (**Figure 6**). To examine the effect of the spinel structure with sulfur anions on the Ni foam substrate, we prepared $NiCo_2S_4$, Ni_3S_2/NF, $NiCo_2O_4$/NF, and bare Ni foam catalysts, and tested their OER activities under identical conditions, also compared with precious metal catalyst IrO_2 on glassy carbon electrode. Linear sweep voltammetry (LSV) polarization curves revealed significant differences in the OER activities of the various electrocatalysts. All potentials were measured against a saturated calomel electrode (SCE) and are reported with respect to a reversible hydrogen electrode (RHE) within the potential range from 1.1 to 1.8 V. In the LSV curves, the ohmic potential drop (iR) arising from the resistance of the electrolyte solution was corrected using the value of R_s obtained using electrochemical impedance spectroscopy (EIS). To estimate and compare the OER performance of the electrocatalysts, we used the overpotential at a current density of 10 mA cm^{-2} and the Tafel slope (log j–η). As revealed in Figure 6a, the $NiCo_2S_4$ NW/NF exhibited a low overpotential of 260 mV (Figure 6b) at the current density of 10 mA cm^{-2} and a Tafel slope of 40.1 mV dec^{-1} (Figure 6c). At the same condition, the IrO_2 catalyst showed an overpotential of 340 mV with a Tafel slope of 72.5 mV dec^{-1}, which is 90 mV higher than that of $NiCo_2S_4$ NW/NF. It clearly revealed the superior activity of $NiCo_2S_4$ NW with Ni foam support. At the same current density, the $NiCo_2S_4$ and bare Ni foam displayed very high overpotentials of 350 and 390 mV, respectively; similarly, the Tafel slopes were also very high (74.5 and 134.2 mV dec^{-1}, respectively). The $NiCo_2O_4$/NF required an overpotential of 330 mV to afford a current density of 10 mA cm^{-2} and a Tafel slope of 66.9 mV dec^{-1}; this overpotential was 70 mV higher than that of $NiCo_2S_4$ NW/NF. For the Ni_3S_2/NF, an overpotential of 300 mV was needed to reach the current density of 10 mA cm^{-2} with a Tafel slope of 51 mV dec^{-1}; this overpotential was intermediate between those of the $NiCo_2O_4$/NF and $NiCo_2S_4$ NW/NF. The anodic peak near 1.36 V in the LSV

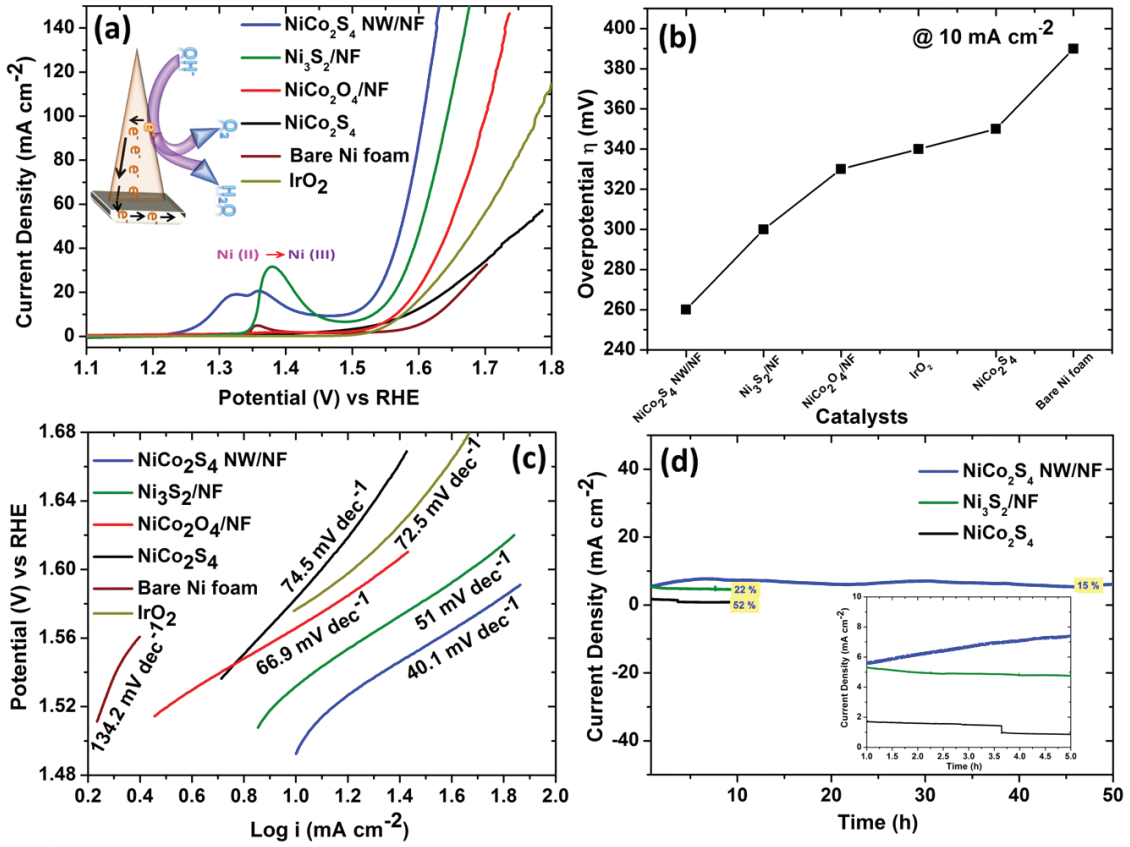

Figure 6. a) OER polarization curves (iR-corrected) of $NiCo_2S_4$ NW/NF, Ni_3S_2/NF, $NiCo_2O_4$/NF, $NiCo_2S_4$, bare Ni foam, and IrO_2 with a scan rate of 10 mV s^{-1}. b) The required overpotential to achieve a current density of 10 mA cm^{-2} for different electrocatalysts. c) Corresponding OER Tafel plots. d) Time dependent current density curves of $NiCo_2S_4$ NW/NF, Ni_3S_2/NF, and $NiCo_2S_4$ at a static potential of 1.527 V versus RHE for 50 h, in 1 M KOH.

of the bare Ni foam was due to a change in the Ni oxidation state from Ni(II) to Ni(III);[43] the same anodic peak was evident for all of the Ni foam-supported electrocatalysts. In addition, the $NiCo_2S_4$ NW/NF exhibited the highest current density and a much earlier onset when compared with those of the other tested electrocatalyst samples. The $NiCo_2S_4$ NW/NF electrocatalyst also afforded a current density of 10 mA cm^{-2} with a relatively low overpotential of 340 mV in 0.1 M KOH (Figure S11, Supporting Information). Taken together, our results reveal that the $NiCo_2S_4$ NW/NF exhibited a very low overpotential and Tafel slope for OER activity when compared with those of the other electrocatalysts. Generally, the favorable OER mechanism of Ni and Co based oxide catalysts has been already proposed in alkaline electrolyte. Accordingly, the development of an active transition metal oxy-hydroxide phase due to the electrochemical tuning of tansition metals in $NiCo_2S_4$ NW/NF.[44] The transition metal oxy-hydroxides undergo OER mechanism as given in the below equation. During this reaction, the formation of an active β-M(IV)-OOH responsible for the efficient oxygen evolution reaction.[45,46] Where, M is the transition metals

$$M(III)OOH+OH^- \rightarrow M(IV)O(OH)_2+e^- \quad (1)$$

$$M(IV)O(OH)_2+OH^- \rightarrow \left[M(IV)O(OH)_2\right]^+ + e^- \quad (2)$$

$$\left[M(IV)O(OH)_2\right]^+ + 2OH^- \rightarrow \left[M(III)O\right]^+ + O_2 + 2H_2O + 2e^- \quad (3)$$

$$\left[M(III)O\right]^+ + OH^- \rightarrow M(III)OOH \quad (4)$$

We attribute the enhancement in OER activity of the $NiCo_2S_4$ NW/NF to several factors. (i) The closely packed arrays of large S^{2-} anions (larger than O^{2-} anions) with Ni and Co metal cations in various valence states (Figure 5) present in the tetrahedral and octahedral sites, respectively, of the spinel crystal structure, resulting in more octahedral active sites of Co(III) cations for efficient OER activity at a very low activation potential.[31] (ii) Although bifunctional activity is mainly correlated to the content of octahedral centers of the electrocatalyst,[47] Ni also has very good electronic conductivity, thereby facilitating electron transfer to the substrate. (iii) The $NiCo_2S_4$ NW/NF nanowire array morphology was itself beneficial for enhancing the OER activity, because these nanowire arrays had grown uniformly on the Ni substrate with good separation (Figure 3); in addition, more active sites were exposed in electrolyte, also improving the OER activity (Figure 4). (iv) The electrochemical surface area of the $NiCo_2S_4$ nanowire arrays on the Ni foam was very high compared with those of the other catalysts. (v) The surface roughness of the $NiCo_2S_4$ NW/NF was very high, allowing it to act as a highly hydrophilic (Figure S5, Supporting Information) catalyst in the electrolyte solution.

(vi) The in situ directional self-growth of the $NiCo_2S_4$ nanowire arrays on the substrate allowed direct contact of the active sites in each nanowire array; the absence of any binder, as used in other methods, that might hinder the kinetics of ion and electron transport helped to decrease the charge transfer resistance (inset to Figure 6a), minimize the contact resistance, and increase the electron paths for efficient electron flow between the nanowire array of the catalyst and the substrate. Because of the $NiCo_2S_4$ NW/NF structure's high hydrophilicity, uniform growth with good separation, identical number of active sites, greater surface area, and higher surface roughness, we suspected that the electrolyte would be able to enter and use the whole catalyst when performing the electrochemical reactions.

In addition to the catalytic activity, we also explored the long-term electrochemical stability of the $NiCo_2S_4$, $NiCo_2S_4$ NW/NF, and Ni_3S_2/NF electrodes for OER in 1 M KOH at a static potential of 1.527 V versus RHE (Figure 6d). At a stable current density of 10 mA cm^{-2}, the $NiCo_2S_4$ NW/NF electrode exhibited 85% of its initial activity retention after 50 h of continuous operation, suggesting excellent durability for OER in extremely alkaline solution. Although we observed vigorous and continuous gas evolution during the electrolysis on the surface of the $NiCo_2S_4$ NW/NF electrode, these gas bubbles dissipated rapidly into the electrolyte and no bubbles remained on the electrode surface. In the durability tests of $NiCo_2S_4$ and Ni_3S_2/NF, we observed losses of greater than 50% and 20% in their current densities within 5 and 10 h, respectively, when applying the same static potential of 1.527 V versus RHE. Clearly, the stability of the spinel $NiCo_2S_4$ NW/NF electrode was greater than those of the other electrocatalysts in 1 M KOH electrolyte. After performing the 50 h OER stability tests, we examined the electrodes using XRD, FESEM, and XPS. In Figure S6b (Supporting Information), the XRD pattern of the $NiCo_2S_4$ NW/NF phase did not feature any major changes. The FESEM images (Figure S7b, Supporting Information) suggested that the morphology of the $NiCo_2S_4$ NW/NF had changed slightly; because OER is a sluggish kinetic reaction that operates at high positive potential with continuous evolution of O_2 gas, it is not unreasonable that small changes in morphology might occur.[6] In the XPS spectra recorded after 50 h, the stable OER electrode appeared to contain the same Co, Ni, and S ions (Figure S9, Supporting Information) as those in the fresh sample. In addition, it featured two extra peaks at 785.4 and 795.7 eV in the Co 2p spectrum, corresponding to the Co $2p_{3/2}$ and Co $2p_{1/2}$ binding energies, respectively, of a $Co(OH)_2$ phase.[9] Likewise, in the Ni 2p spectrum, a signal for NiOOH was present at 857.7 eV. These two phases are known active sites for enhanced OER activity.[33] Because of such hydroxide formation during OER, we observed an intense peak for oxygen atoms in the O 1s spectrum. This very slight change in the valence state at the surface was consistent with the high stability of the $NiCo_2S_4$ NW/NF electrode.

To explore the suitability of $NiCo_2S_4$ NW/NF catalysts in the full water splitting process, we also assessed the electrocatalytic HER performance of all samples in 1 M KOH electrolyte solution using LSV in a three-electrode system; **Figure 7** presents the results. We applied iR correction to all of our data. Figure 7a presents the polarization curves of $NiCo_2S_4$ NW/NF, Ni_3S_2/NF, $NiCo_2O_4$/NF, bare Ni foam, and Pt/C (40%). $NiCo_2S_4$ NW/NF

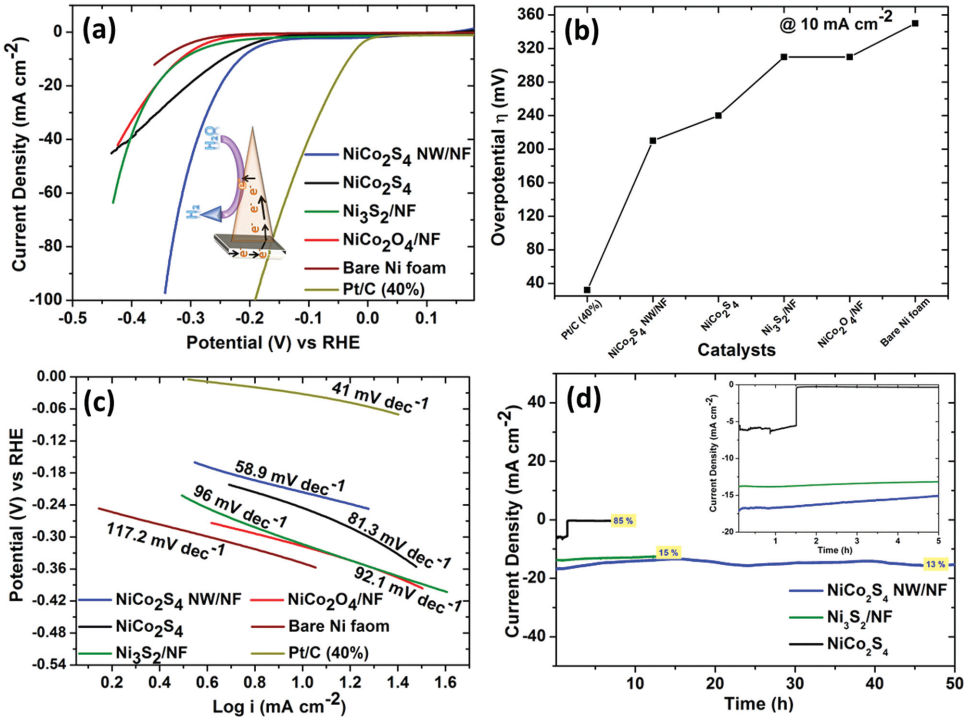

Figure 7. a) HER polarization curves (iR-corrected) of $NiCo_2S_4$ NW/NF, Ni_3S_2/NF, $NiCo_2O_4$/NF, $NiCo_2S_4$, bare Ni foam, and Pt/C (40%) with a scan rate of 10 mV s^{-1}. b) The required overpotential to achieve a current density of 10 mA cm^{-2} for different electrocatalysts. c) Corresponding Tafel Plots of HER. d) Time-dependent current density curves of $NiCo_2S_4$ NW/NF, Ni_3S_2/NF, and $NiCo_2S_4$ at a static potential of –0.323 V versus RHE for 50 h, in 1 M KOH.

required a very low overpotential of 210 mV to deliver the current density of 10 mA cm^{-2}. The overpotential for $NiCo_2S_4$ was also relatively low (240 mV); thus, it also appeared to be a highly active electrocatalyst for HER in a strong alkaline electrolyte. The Ni_3S_2/NF and $NiCo_2O_4$/NF both required the same overpotential of 310 mV to afford a current density of 10 mA cm^{-2}. Although the bare Ni foam was also electroactive toward HER, it required a very high overpotential of 350 mV to produce a current density of 10 mA cm^{-2}. In the case of precious catalyst Pt/C (40%) needed very low overpotential of 32 mV to afford 10 mA cm^{-2} with lower Tafel slope of 41 mV dec^{-1}, which may be due to the higher percentage (40%) of platinum on carbon. In common, the hydrogen evolution was achieved by transition metal chalcogenides in the alkaline medium under the Tafel–Volmer–Heyrosky mechanism (Equations (5)–(7)).[48] The crucial role of the formation of transition chalcogenide hydrides ($M_{cat}H_{chem}$) is the rate determining step (Tafel–Volmer step, Equation (6)). The $NiCo_2S_4$ NW/NF possessed high HER activity due to the favorable Tafel–Volmer step, which helps to start the hydrogen evolution at low overpotential in alkaline medium.

$$2M_{cat}H_{chem} \rightleftharpoons H_2 + M_{cat}\,(\text{Tafel}) \quad (5)$$

$$M_{cat} + H_2O + e^- M_{cat} \rightleftharpoons H_{chem} + OH^-\,(\text{Volmer}) \quad (6)$$

$$M_{cat}H_{chem} + H_2O + e^- \rightleftharpoons H_2 + M_{cat} + OH^-\,(\text{Heyrovsky}) \quad (7)$$

Again, we attribute the superior activity of the $NiCo_2S_4$ NW/NF to the in situ growth of the $NiCo_2S_4$ electrocatalyst on the Ni foam without any binder; it not only enhanced the mechanical adhesion and electrical conductivity (inset to Figure 7a) but also led to uniform growth of the catalyst with a larger electrochemical surface area and greater number of active sites available for electrochemical redox reactions.[32] Figure 7b presents the overpotentials required for all of the electrocatalysts to afford a current density of 10 mA cm^{-2} in 1 M KOH; Figure 7c provides corresponding Tafel plots. We fitted the linear regions in the LSV curves of all of the samples to the Tafel equation to measure the corresponding Tafel slopes. The Tafel slope of the $NiCo_2S_4$ NW/NF (58.9 mV dec^{-1}) was lower than those of the other electrocatalysts: 81.3, 96, 92.1, and 117.2 mV dec^{-1} for $NiCo_2S_4$, Ni_3S_2/NF, $NiCo_2O_4$/NF, and the bare Ni foam, respectively. Thus, the Tafel slope also reveals the better HER performance of the $NiCo_2S_4$ NW/NF, in good agreement with the LSV data.

We tested the long-term HER electrochemical stability of the $NiCo_2S_4$ NW/NF through continuous electrolysis at a static potential of –0.323 V versus RHE, with an initial current density of 18 mA cm^{-2} (Figure 7d). The current density decreased slightly (by ≈10%) after 50 h of electrolysis with continuous gas evolution on the electrode surface. We observed no changes in the XRD patterns (Figure S6c, Supporting Information) and FESEM images (Figure S8b, Supporting Information) of the $NiCo_2S_4$ NW/NF before and after the 50 h continuous HER durability test, confirming that the structure maintained its phase and morphology. In addition, the XPS spectra of the $NiCo_2S_4$ NW/NF recorded after the durability test (Figure S10, Supporting Information) was similar to that recorded initially, with similar peaks in the Co 2p, Ni 2p, and S 2p spectra, suggesting only very small changes in the valence state. The XPS data suggested good stability of the $NiCo_2S_4$ NW/NF during HER in 1 M KOH electrolyte. Notably, the $NiCo_2S_4$ NW/NF was also more stable under the negative cathodic potential during HER.

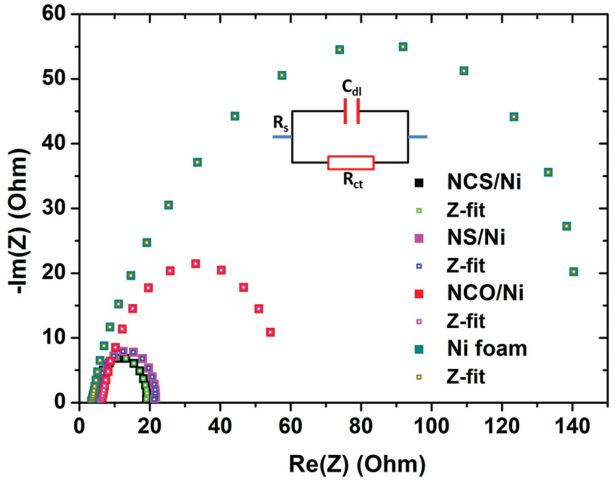

Figure 8. Nyquist plots of bare Ni foam, $NiCo_2S_4$ NW/NF, Ni_3S_2/NF, and $NiCo_2O_4$/NF electrodes recorded at an applied potential of 0.5 V with a frequency range of 200 kHz to 10 mHz in 1 M KOH.

The ionic and transport resistances are also essential factors affecting the OER and HER activities in an electrolyte. To determine the roles played by these resistances during the OER and HER, we recorded Nyquist plots at 0.5 V (**Figure 8**) and open circuit voltage (OCV) (Figure S2, Supporting Information). We used the Randles equivalent circuit to obtain the values of the ionic and charge transfer resistances of the OER and HER catalyst in 1 M KOH electrolyte (insets). Here, R_s is the resistance of the electrolyte; C_{dl} and R_{ct} are the double-layer capacitance and charge transfer resistance, respectively, of the catalyst in the electrolyte.[2] In the high frequency region, the low value of R_s of 6.5 Ω is related to the uncompensated solution resistance; it was comparable for all of the catalysts at 0.5 V (Figure 8) and OCV (Figure S2, Supporting Information). In Figure 8, at 0.5 V potential, the charge transfer resistance (R_{ct}) in the lower frequency region was determined from the fitted values for the equivalent circuit. Together, these values allowed us to interpret the reaction kinetics of the catalysts. The hierarchical $NiCo_2S_4$ NW/NF displayed a charge transfer resistance of ≈18 Ω; the value for the Ni_3S_2/NF was slightly higher (24 Ω), but still low. The $NiCo_2O_4$/NF had an intermediate-value charge transfer resistance of 58 Ω, while the bare Ni foam possessed a very high charge transfer resistance of 142 Ω in the electrolyte. We attribute the enhanced electrical conductivities of the $NiCo_2S_4$ NW/NF and Ni_3S_2/NF to the existence of nickel, a highly electron transporting element, in the catalyst.[49] The resistances acquired from the EIS spectra of the various catalysts revealed that the $NiCo_2S_4$ NW/NF had a significantly lower impedance and, thus, remarkably increased OER kinetics.

We determined the electrochemically active surface area (ECSA) of the $NiCo_2S_4$ NW/NF nanowire array catalyst through electrical double-layer capacitance (EDLC) measurements in 1 M KOH electrolyte (**Figure 9**). Cyclic voltammograms (CV) recorded at various scan rates (10, 30, 50, and 70 mV s^{-1}) are

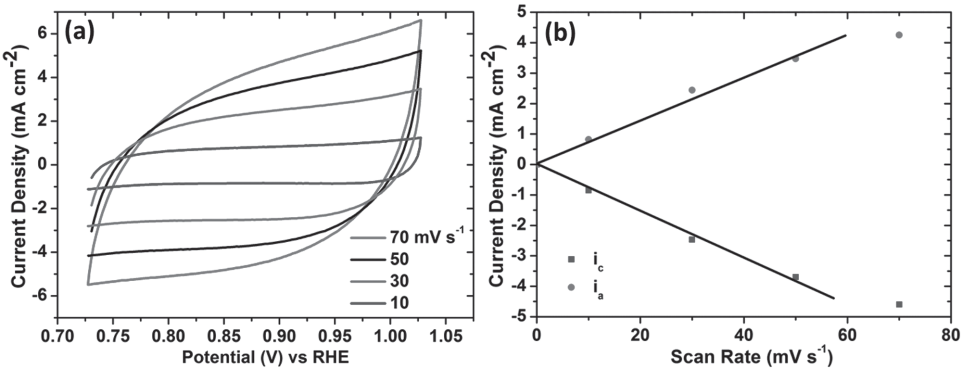

Figure 9. a) Cyclic voltammograms for $NiCo_2S_4$ NW/NF. b) The capacitive currents at 0.875 V versus RHE with a scan rate of 10, 30, 50, and 70 mV s^{-1} in 1 M KOH.

displayed in Figure 9a. For better interpretation and comparison of ECSAs, we also measured the double-layer capacitance behavior of the other catalysts at the same scan rates (Figure S3, Supporting Information). At each scan rate, the $NiCo_2S_4$ NW/NF catalyst provided much higher anodic (i_a) and cathodic (i_c) current densities (CV areas) than those of the other catalysts, consistent with a much greater active surface area. From the CV curves, we measured the values of i_a and i_c at a potential of 0.875 V versus RHE; they are plotted with respect to the scan rate in Figure 9b. From these linear plots, we calculated values for the capacitances of $NiCo_2S_4$ NW/NF, Ni_3S_2/NF, $NiCo_2O_4$/NF, and the bare Ni foam of 40, 6.9, 19.4, and 2.6 mF cm^{-2}, respectively. The considerably higher capacitance of the $NiCo_2S_4$ NW/NF suggested that it had the highest electrochemical surface area and, correspondingly, the highest surface roughness, when compared with those of the other catalysts.[50] Therefore, we attribute the superior OER and HER activities of the $NiCo_2S_4$ NW/NF to the in situ growth of the catalyst on the substrate contributing to the significantly enhanced surface area and number of electrochemically active sites.[51]

We analyzed the wettability of the $NiCo_2S_4$ NW/NF electrode using a water droplet (100 µL) and the static contact angle method, and compared it with that of the bare Ni foam (Figure S4, Supporting Information). In the absence and presence of catalyst coatings, substrates can exhibit different behavior toward water droplets based on their surface roughnesses. As expected, the contact angle of the bare Ni foam was ≈110° (Figure S4a, Supporting Information), indicating its hydrophobic nature. In contrast, the average contact angle of the $NiCo_2S_4$ NW/NF was ≈15° (Figure S4b, Supporting Information), suggesting an extremely hydrophilic surface. These values are in close agreement with previously reported values.[52] The contact angle of a water droplet is influenced by the roughness of its surface, which may amplify the wettability characteristics of a catalyst. Our results suggested that the $NiCo_2S_4$ NW/NF surface was rougher than the bare Ni foam, a favorable structure for greater access of the electrolyte into the catalyst, thereby enhancing the OER and HER performance in an alkaline aqueous electrolyte.

All of the experiments described above suggested that the $NiCo_2S_4$ NW/NF would be an active and stable electrocatalyst for both OER and HER in strong alkaline electrolytes. Therefore, we constructed a two-electrode electrolyzer system using the $NiCo_2S_4$ NW/NF as both the anode and cathode ($NiCo_2S_4$ NW/NF//$NiCo_2S_4$ NW/NF) to go one step closer to a real overall water-splitting system in 1 M KOH. As a control, we prepared electrolyzers having the structures Ni_3S_2/NF//Ni_3S_2/NF, $NiCo_2O_4$/NF//$NiCo_2O_4$/NF, and bare Ni foam//bare Ni foam. **Figure 10**a displays the OER polarization (LSV) curves of all four samples. The performance of the $NiCo_2S_4$ NW/NF//$NiCo_2S_4$

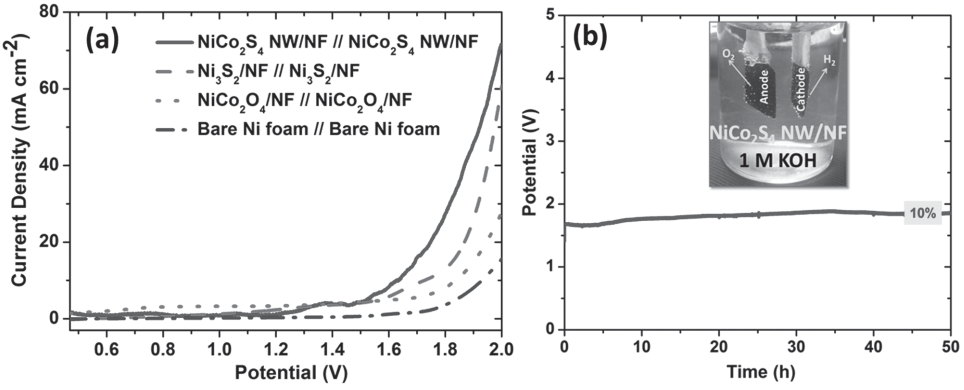

Figure 10. a) Two electrode OER polarization curves (without iR compensation) of $NiCo_2S_4$ NW/NF//$NiCo_2S_4$ NW/NF, Ni_3S_2/NF//Ni_3S_2/NF, $NiCo_2O_4$/NF//$NiCo_2O_4$/NF, and bare Ni foam//bare Ni foam with a scan rate 10 mV s^{-1}. b) Two-electrode cell durability of $NiCo_2S_4$ NW/NF // $NiCo_2S_4$ NW/NF, electrode image with gas evolution (inset) in 1 M KOH. The size of both the electrodes is 1 cm × 1 cm.

Table 1. Comparison of two electrode water splitting cell voltage of $NiCo_2S_4$ NW/NF electrocatalyst with other nonprecious bifunctional electrocatalyst in 1 M KOH.

Catalyst	Support	Overall voltage [V]) @ −10 mA cm^{-2}	Durability	Reference
$NiCo_2S_4$ NW	Ni foam	1.63 V	50 h	This work
Ni_3S_2	Ni foam	1.73 V	–	This work
$NiCo_2O_4$	Ni foam	1.84 V	–	This work
$Ni_{2.3\%}$-CoS_2	Carbon Cloth	1.66 V	12 h	[53]
NiS	Ni foam	1.64 V	20 h	[21]
a-CoSe film	Ti mesh	1.65 V	26 h	[54]
$NiCo_2S_4$	Carbon Cloth	1.68 V	10 h	[29]
$Ni_{0.33}Co_{0.67}S_2$ NWs	Ti foil	1.65 V (5 mA cm^{-2})	20 h	[55]
Ni_3Se_2	Cu foil	1.65 V	12 h	[30]
Ni_2P NPs	Ni foam	1.63 V	10 h	[56]

NW/NF alkaline water electrolyzer was higher than those of the others; it needed a cell voltage of 1.63 V to afford a water splitting current density of 10 mA cm^{-2} with vigorous gas evolution on both electrodes (Figure 10b, inset). In contrast, to achieve current densities of 10 mA cm^{-2}, the Ni_3S_2/NF//Ni_3S_2/NF, $NiCo_2O_4$/NF//$NiCo_2O_4$/NF, and bare Ni foam//bare Ni foam electrolyzers required higher cell voltages of 1.73, 1.84, and 1.93 V, respectively. Notably, the water splitting voltage of the $NiCo_2S_4$ NW/NF//$NiCo_2S_4$ NW/NF device (1.63 V) is lower than those recently reported for Ni_3Se_2/Cu foam (1.65 V)[37] and $NiCo_2S_4$/CC (1.68 V)[33] (**Table 1**). We also tested the long-term durability of the $NiCo_2S_4$ NW/NF//$NiCo_2S_4$ NW/NF electrolyzer for 50 h in 1 M KOH electrolyte. At the onset, a potential of 1.63 V was required to give a current density of 10 mA cm^{-2}; after 50 h of continuous electrolysis testing, negligible decay (≈10% loss) occurred in the value of the static potential.

Solar energy is one of the most powerful sources for the production of electricity through various techniques. The direct use of solar energy to produce hydrogen fuel through water photolysis is a promising means of energy conversion and storage.[57] Accordingly, we wished to employ solar energy directly to form the electricity necessary to split water (**Figure 11**; Figure S12, Supporting Information). Here, we used a commercially available GaAs thin film solar cell panel, which could produce a maximum voltage of 3.65 V with respect to the intensity of incident light. Because of its high open circuit voltage and current density (Figure S13, Supporting Information), it produced sufficient voltage for continuous operation of the water electrolyzer. We used an LED desk night-light as the light source (18 W), implying that we could possibly use night light energy for hydrogen conversion. As displayed in Figure 11, we connected the positive and negative terminals of the solar panel directly to a two-electrode water electrolyzer set-up through a less-resistive crocodile clip. To optimize and monitor the voltage applied to the cell set-up, we connected a digital multimeter through the same crocodile clip (Figure S12, Supporting Information). Finally, we applied a stable potential of 1.68 V (monitored by the digital multimeter) to the water electrolyzer set-up by maintaining a constant distance between the light and the solar panel (Figure S12, Supporting Information). At this potential, we observed continuous evolution of oxygen and hydrogen gas on the anode and cathode, respectively (Movie S1, Supporting Information). This small demonstration gives hope for greater exploration of hierarchical $NiCo_2S_4$ nanowire arrays on Ni foam as a means toward the development of real, large-scale solar-to-hydrogen generation.

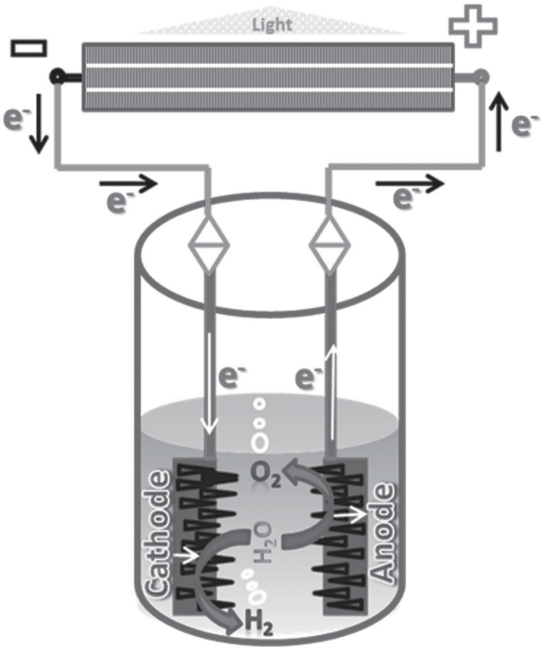

Figure 11. Solar energy derived water electrolysis (Two electrodes cell of $NiCo_2S_4$ NW/NF as an anode and $NiCo_2S_4$ NW/NF as a cathode in 1 M KOH).

3. Conclusion

We have explored in situ-grown 1D $NiCo_2S_4$ nanowire arrays on 3D Ni foams as efficient bifunctional electrocatalysts in strongly alkaline electrolytes. Because of its high surface area, well-separated nanowire structure and uniform growth, and enhanced charge transport, the binder-free self-made $NiCo_2S_4$ NW/NF electrode delivered a mass hydrogen production current density of 10 mA cm^{-2} at low overpotentials of 260 mV for OER and 210 mV for HER in 1 M KOH. Furthermore, the $NiCo_2S_4$ NW/NF could produce stable hydrogen and oxygen evolution at low overpotentials over long periods of time. When used in an alkaline water electrolyzer, the nonprecious-metal $NiCo_2S_4$ NW/NF afforded vigorous and continuous evolution of H_2 and O_2 at a current density of 10 mA cm^{-2} under a cell voltage of 1.63 V. This demonstration of solar-to-hydrogen generation through overall water splitting is the first example for this bifunctional electrocatalyst. The excellent bifunctional activity and superior stability of our in situ, inexpensive, earth-abundant electrocatalyst suggests

that it could be a promising candidate structure for use in water splitting devices for large scale solar-to-hydrogen generation.

4. Experimental Section

Materials: Nickel nitrate hexahydrate [$Ni(NO_3)_2{\cdot}6H_2O$] and urea (CH_4N_2O) were purchased from Sigma-Aldrich. Cobalt nitrate hexahydrate [$Co(NO_3)_2{\cdot}6H_2O$] and sodium sulfide hydrate ($Na_2S{\cdot}xH_2O$) were purchased from Alfa Aesar. These chemicals were used as received without further purification. Deionized (DI) water, ethanol, and 3 M HCl were used as solvents and for washing. The Ni foam (thickness: 0.08 mm) was purchased from MTI Korea. To remove the surface oxidized layer, a piece of Ni foam (2 cm × 3 cm) was cleaned through sonication consecutively in 3 M HCl, ethanol, and DI water (5 min each) prior to using as a substrate.

$NiCo_2S_4$ NW/NF Electrocatalyst: A solution of 0.004 M nickel nitrate and 0.008 M cobalt nitrate was prepared in DI water (30 mL) with stirring. 0.012 M Urea was added to this solution as a reducing agent with stirring and then the mixture was stirred for 15 min to obtain a clear solution. This mixed solution was transferred into Teflon-lined stainless-steel 50 mL autoclave. For in situ growth of the catalyst, the surface-cleaned Ni foam was immersed into the solution. The autoclave was locked tightly and maintained at 120 °C for 8 h in an electric oven. After a certain period, the uniformly grown Ni–Co-carbonates hydroxide nanowire arrays on Ni foam were removed from the solution and washed several times with DI water to remove any unreacted residues.

Sodium sulfide flakes were used to prepare a 0.2 M solution in DI water (30 mL) while stirring for 10 min. This sulfide precursor solution was transferred to the same autoclave, containing the Ni-Co-carbonates hydroxide nanowire arrays grown on Ni foam, and maintained at 160 °C for 8 h in an electric oven. After cooling to room temperature, the $NiCo_2S_4$ nanowire arrays grown on the Ni foam ($NiCo_2S_4$ NW/NF) were washed several times with ethanol and DI water, followed by drying at 60 °C overnight in the vacuum oven. $NiCo_2S_4$ was also prepared using the same conditions, but without the Ni foam.

For comparison of catalytic activities, Ni_3S_2 on Ni foam (Ni_3S_2/NF) was prepared using the same method and parameters, but without the cobalt precursor. To prepare $NiCo_2O_4$ on Ni foam ($NiCo_2O_4$/NF), after the first step the Ni-Co-carbonates hydroxide nanowire arrays were annealed at 450 °C for 2 h in air to completely convert the structure into $NiCo_2O_4$; the second step in the hydrothermal growth process was not efficient at converting the Ni-Co-carbonates hydroxide nanowire arrays completely into $NiCo_2O_4$ in the DI water environment.

Characterization: The phase formation was identified using powder XRD (Rigaku, MiniFlex 600) with Cu Kα radiation (λ = 1.5418 Å). The morphologies of the catalysts were observed using FESEM (Hitachi-S4800) at an accelerating voltage of 3 kV. More detailed information regarding the morphologies, the various elements present in the rods, and the crystallinity was obtained using HRTEM (Hitachi HF-3300, 300 kV). XPS measurements were performed on catalyst samples to determine the oxidation states and chemical bonding between the elements, using a Thermo-Scientific ESCALAB 250Xi apparatus, a vacuum of 10^{-9} mbar, and Mg as the exciting source. Hydrophilicity was measured using a contact angle measurement system.

Electrochemical Measurements: Electrochemical tests were performed using an electrochemistry workstation (Bio-Logic). The various catalysts grown on Ni foam and the catalyst ink cast on glassy carbon were used as the working electrode; a platinum wire was the counter electrode; a saturated calomel electrode was the reference electrode. All measurements were performed in 1 M KOH aqueous electrolyte at a scan rate of 10 mV s^{-1} to minimize the capacitive current. All of the potentials in the LSV polarization curves were iR-corrected with respect to the ohmic resistance of the solution, unless specifically indicated. Because the Ni foam might have dissolved during hydrothermal synthesis, due to decomposition of urea in the aqueous environment,[58] accurate measurement of the catalyst loading on the Ni foam was challenging. Therefore, the reported current density was based on the geometrical area. EIS was performed with the working electrode nonbiased or biased at a certain potential while sweeping the frequency from 100 kHz to 10 mHz. The measured impedance data were fitted to a simplified Randles circuit to extract the series and charge transfer resistances. The electrochemical surface area for working electrode was measured at various scan rates. The overall water splitting test was performed in a two-electrode system, with two symmetric catalyst electrodes as both the anode and cathode. In the same two-electrode system, a solar panel was used as a voltage source for solar-to-hydrogen generation. All potentials reported in this work were against the RHE, which was converted from the SCE scale using a calibration. The surface roughness and hydrophilicity of the samples were measured in terms of droplet wettability (static contact angle method).

Supporting Information

Supporting Information is available from the Wiley Online Library or from the author.

Acknowledgements

This work is financially supported by the DGIST R&D Program of the Ministry of Science, ICT and Future Planning of Korea (16- RS-04).

Received: February 1, 2016
Revised: February 26, 2016
Published online: April 9, 2016

[1] C. Ouyang, X. Wang, C. Wang, X. Zhang, J. Wu, Z. Ma, S. Dou, S. Wang, *Electrochim. Acta* **2015**, *174*, 297.
[2] H. Cheng, Y. Z. Su, P. Y. Kuang, G. F. Chen, Z. Q. Liu, *J. Mater. Chem. A* **2015**, *3*, 19314.
[3] H. Wang, H. W. Lee, Y. Deng, Z. Lu, P. C. Hsu, Y. Liu, D. Lin, Y. Cui, *Nat. Commun.* **2015**, *6*, 7261.
[4] X. Zhang, H. Xu, X. Li, Y. Li, T. Yang, Y. Liang, *ACS Catal.* **2016**, *6*, 580.
[5] L. Kuai, J. Geng, C. Chen, E. Kan, Y. Liu, Q. Wang, B. Geng, *Angew. Chem. Int. Ed.* **2014**, *53*, 7547.
[6] X. Lv, Y. Zhu, H. Jiang, X. Yang, Y. Liu, Y. Su, J. Huang, Y. Yao, C. Li, *Dalton Trans.* **2015**, *44*, 4148.
[7] M. Gong, W. Zhou, M. J. Kenney, R. Kapusta, S. Cowley, Y. Wu, B. Lu, M. C. Lin, D. Y. Wang, J. Yang, B. J. Hwang, H. Dai, *Angew. Chem. Int. Ed.* **2015**, *54*, 11989.
[8] P. D. Tran, M. Nguyen, S. S. Pramana, A. Bhattacharjee, S. Y. Chiam, J. Fize, M. J. Field, V. Artero, L. H. Wong, J. Loo, J. Barber, *Energy Environ. Sci.* **2012**, *5*, 8912.
[9] C. Tang, N. Cheng, Z. Pu, W. Xing, X. Sun, *Angew. Chem. Int. Ed.* **2015**, *54*, 9351.
[10] K. Zeng, D. Zhang, *Prog. Energy Combust. Sci.* **2010**, *36*, 307.
[11] X. Liu, S. Cui, Z. Sun, P. Du, *Chem. Commun.* **2015**, *51*, 12954.
[12] H. Vrubel, X. Hu, *Angew. Chem. Int. Ed.* **2012**, *51*, 12703.
[13] Y. Liu, H. Wang, D. Lin, C. Liu, P. C. Hsu, W. Liu, W. Chen, Y. Cui, *Energy Environ. Sci.* **2015**, *8*, 1719.
[14] C. C. L. McCrory, S. Jung, I. M. Ferrer, S. M. Chatman, J. C. Peters, T. F. J. Jaramillo, *J. Am. Chem. Soc.* **2015**, *137*, 4347.
[15] S. Yagi, I. Yamada, H. Tsukasaki, A. Seno, M. Murakami, H. Fujii, H. Chen, N. Umezawa, H. Abe, N. Nishiyama, S. Mori, *Nat. Commun.* **2015**, *6*, 1.
[16] Y. Zhao, B. Sun, X. Huang, H. Liu, D. Su, K. Sun, G. Wang, *J. Mater. Chem. A* **2015**, *3*, 5402.

[17] Y. Zhao, S. Chen, B. Sun, D. Su, X. Huang, H. Liu, Y. Yan, K. Sun, G. Wang, *Sci. Rep.* **2015**, *5*, 1.
[18] M. Gong, H. Dai, *Nano Res.* **2015**, *8*, 23.
[19] M. Prabu, K. Ketpang, S. Shanmugam, *Nanoscale* **2014**, *6*, 3173.
[20] R. Chen, H. Y. Wang, J. Miao, H. Yang, B. Liu, *Nano Energy* **2015**, *11*, 333.
[21] W. Zhu, X. Yue, W. Zhang, S. Yu, Y. Zhang, J. Wang, J. Wang, *Chem. Commun.* **2016**, *52*, 1486.
[22] M. S. Burke, M. G. Kast, L. Trotochaud, A. M. Smith, S. W. Boettcher, *J. Am. Chem. Soc.* **2015**, *137*, 3638.
[23] B. You, N. Jiang, M. Sheng, M. W. Bhushan, Y. Sun, *ACS Catal.* **2016**, *6*, 714.
[24] R. Chen, G. Sun, C. Yang, L. Zhang, J. Miao, H. Tao, H. Yang, J. Chen, P. Chen, B. Liu, *Nanoscale Horiz.* **2016**, *1*, 156.
[25] P. Ganesan, M. Prabu, J. Sanetuntikul, S. Shanmugam, *ACS Catal.* **2015**, *5*, 3625.
[26] B. Lu, D. Cao, P. Wang, G. Wang, Y. Gao, *Int. J. Hydrogen Energy* **2011**, *36*, 72.
[27] J. Yin, P. Zhou, L. An, L. Huang, C. Shao, J. Wang, H. Liua, P. Xi, *Nanoscale* **2016**, *8*, 1390.
[28] J. Huang, D. Hou, Y. Zhou, W. Zhou, G. Li, Z. Tang, L. Lia, S. Chen, *J. Mater. Chem. A* **2015**, *3*, 22886.
[29] D. Liu, Q. Lu, Y. Luo, X. Sun, A. M. Asiri, *Nanoscale* **2015**, *7*, 15122.
[30] J. Shi, J. Hu, Y. Luo, X. Sun, A. M. Asiri, *Catal. Sci. Technol.* **2015**, *5*, 4954.
[31] Z. Zhang, X. Wang, G. Cui, A. Zhang, X. Zhou, H. Xu, L. Gu, *Nanoscale* **2014**, *6*, 3540.
[32] J. B. Wu, Z. G. Li, X. H. Huang, Y. Lin, *J. Power Sources* **2013**, *224*, 1.
[33] H. Chen, J. Jiang, L. Zhang, D. Xia, Y. Zhao, D. Guo, T. Qi, H. Wan, *J. Power Sources* **2014**, *254*, 249.
[34] B. Yang, L. Yu, H. Yan, Y. Sun, Q. Liu, J. Liu, D. Song, S. Hu, Y. Yuan, L. Liub, J. Wang, *J. Mater. Chem. A* **2015**, *3*, 13308.
[35] J. Yang, C. Yu, X. Fan, C. Zhao, J. Qiu, *Adv. Funct. Mater.* **2015**, *25*, 2109.
[36] S. Yang, B. Deng, R. Ge, L. Zhang, H. Wang, Z. Zhang, W. Zhu, G. Wang, *Nanoscale Res. Lett.* **2014**, *9*, 672.
[37] B. Zhu, S. Tang, S. Vongehr, H. Xie, J. Zhu, X. Meng, *Chem. Commun.* **2016**, *52*, 2624.
[38] W. Zhou, X. J. Wu, X. Cao, X. Huang, C. Tan, J. Tian, H. Liu, J. Wang, H. Zhang, *Energy Environ. Sci.* **2013**, *6*, 2921.
[39] W. Kong, C. Lu, W. Zhang, J. Pub, Z. Wang, *J. Mater. Chem. A* **2015**, *3*, 12452.
[40] Y. Liu, J. Zhang, S. Wang, K. Wang, Z. Chen, Q. Xu, *New J. Chem.* **2014**, *38*, 4045.
[41] L. Mi, W. Wei, S. Huang, S. Cui, W. Zhang, H. Hou, W. Chen, *J. Mater. Chem. A* **2015**, *3*, 20973.
[42] W. Wei, L. Mi, S. Cui, B. Wang, W. Chen, *ACS Sustainable Chem. Eng.* **2015**, *3*, 2777.
[43] M. Q. Yu, Y. H. Li, S. Yang, P. F. Liu, L. F. Pan, L. Zhang, H. G. Yang, *J. Mater. Chem. A* **2015**, *3*, 14101.
[44] W. Chen, H. Wang, Y. Li, Y. Liu, J. Sun, S. Lee, J. S. Lee, Y. Cui, *ACS Cent. Sci.* **2015**, *1*, 244.
[45] M. E. G. Lyons, M. P. Brandon, *Int. J. Electrochem. Sci.* **2008**, *3*, 1386.
[46] P. Chen, K. Xu, Z. Fang, Y. Tong, J. Wu, X. Lu, X. Peng, H. Ding, C. Wu, Y. Xie, *Angew. Chem. Int. Ed.* **2015**, *54*, 14710.
[47] J. Suntivich, K. J. May, H. A. Gasteiger, J. B. Goodenough, Y. S. Horn, *Science* **2011**, *334*, 1383.
[48] R. Jervis, N. Mansor, C. Gibbs, C. A. Murray, C. C. Tang, P. R. Shearing, D. J. L. Brett, *J. Electrochem. Soc.* **2014**, *161*, 458.
[49] Y. Meng, W. Song, H. Huang, Z. Ren, S. Y. Chen, S. L. Suib, *J. Am. Chem. Soc.* **2014**, *136*, 11452.
[50] X. Dai, K. Du, Z. Li, M. Liu, Y. Ma, H. Sun, X. Zhang, Y. Yang, *ACS Appl. Mater. Interfaces* **2015**, *7*, 27242.
[51] V. H. Nguyen, J. J. Shim, *Electrochim. Acta* **2015**, *166*, 302.
[52] W. J. Khudhayer, R. Sharma, T. Karabacak, *Nanotechnology* **2009**, *20*, 275302.
[53] W. Fanga, D. Liua, Q. Lua, X. Sunb, A. M. Asir, *Elelctrochem. Commun.* **2016**, *63*, 60.
[54] T. Liu, Q. Liu, A. M. Asiri, Y. Luo, X. Sun, *Chem. Commun.* **2015**, *51*, 16683.
[55] Z. Peng, D. Jia, A. M. Al-Enizi, A. A. Elzatahry, G. Zheng, *Adv. Energy Mater.* **2015**, *5*, 1402031.
[56] L. A. Stern, L. Feng, F. Song, X. Hu, *Energy Environ. Sci.* **2015**, *8*, 2347.
[57] J. Li, Y. C. Wang, T. Zhou, H. Zhang, X. Sun, J. Tang, L. Zhang, A. M. Al-Enizi, Z. Yang, G. Zheng, *J. Am. Chem. Soc.* **2015**, *137*, 14305.
[58] X. Tong, X. Xia, C. Guo, Y. Zhang, J. Tu, H. J. Fan, X. Y. Guo, *J. Mater. Chem. A* **2015**, *3*, 18372.